Correlation notice on the electrochemical dealloying and antibacterial properties of gold–silver alloy nanoparticles

Javad B. M. Parambath · Islam M. Ahmady · Seema Panicker ·
Aebin Sin · Changseok Han · Ahmed A. Mohamed

Abstract Galvanic replacement reaction was used in the synthesis of bimetallic gold–silver alloy nanoparticles (Au–Ag NPs), where pre-synthesized Ag nanoparticles-polyvinylpyrrolidone (AgNPs-PVP) were used to reduce the aryldiazonium tetrachloroaurate(III) salt in water. TEM images and EDS elemental analysis showed the formation of spherical Au–Ag NPs with sizes of 12.8 ± 4.9 nm and 25.6 ± 14.4 nm for corresponding Au–Ag ratios and termed as $Au_{0.91}Ag_{0.09}$ and $Au_{0.79}Ag_{0.21}$, respectively, with different concentrations of the gold precursor. The hydrodynamic sizes measured using dynamic light scattering are 46.4 nm and 74.8 nm with corresponding zeta potentials of -44.56 and -25.09 mV in water, for $Au_{0.91}Ag_{0.09}$ and $Au_{0.79}Ag_{0.21}$ respectively. Oxidative leachability of Ag ion studies from the starting AgNPs-PVP in 1 M NaCl showed a significant decrease in the plasmon peak after 8 h, indicating the complete dissolution of Ag ions, however, there is enhanced oxidation resistivity of Ag from Au–Ag NPs even after 24 h. Electrochemical studies on glassy carbon electrodes displayed a low oxidation peak in aqueous solutions of 20 mM KCl at 0.16 V and KNO_3 at 0.33 V vs. saturated calomel electrode (SCE). We studied the antibacterial activity of Au–Ag alloy nanoparticles against gram-positive *Staphylococcus aureus, Staphylococcus epidermidis, Enterococcus faecalis,* and gram-negative *Escherichia coli*, *Salmonella typhimurium,* and *Pseudomonas aeruginosa*. Our findings demonstrated superior antibacterial activity of Au–Ag NPs compared with AgNPs-PVP. Moreover, the nanoparticles inhibited the *S. epidermidis* biofilm formation.

J. B. M. Parambath · S. Panicker · A. A. Mohamed (✉)
Department of Chemistry, University of Sharjah,
Sharjah 27272, United Arab Emirates
e-mail: ah.mohamed@sharjah.ac.ae

J. B. M. Parambath
e-mail: jbasil@sharjah.ac.ae

S. Panicker
e-mail: seemasooraj25@gmail.com

I. M. Ahmady
Department of Applied Biology, University of Sharjah,
Sharjah 27272, United Arab Emirates
e-mail: ialtayeb@sharjah.ac.ae

A. Sin · C. Han
Program in Environmental & Polymer Engineering,
Graduate School, INHA University, Incheon 22212,
Republic of Korea
e-mail: aebinsin@inha.edu

C. Han
e-mail: hanck@inha.ac.kr

C. Han
Department of Environmental Engineering, INHA
University, Incheon 22212, Republic of Korea

Graphical abstract
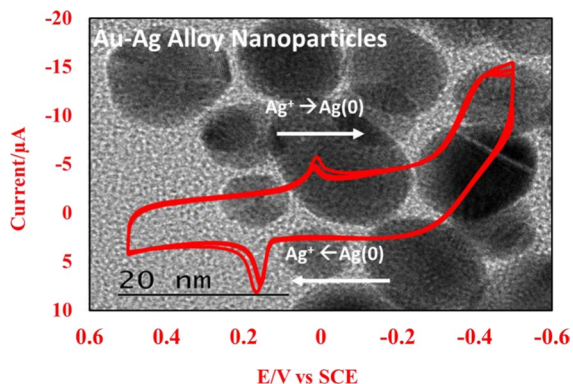
Introduction

The interest in gold–silver nanostructures originated from the old civilizations (Botros 2015). The curiosity in developing such nanostructures takes its roots from the natural alloy "Electrum" which contains different ratios of gold and silver metals. Moreover, the different routes for the synthesis of Au–Ag nanostructures published in recent years have been increasing rapidly because of their stoichiometric control which resulted in several applications (Link et al. 1999; Ferrando et al. 2008; Chernousova and Epple 2013; Cunningham et al. 2016; Gilroy et al. 2016; Zugic et al. 2017; Shirman et al. 2018; Wang et al. 2018; Bijalwan et al. 2020; Borah and Verbruggen 2020; Zhou et al. 2020; Loza et al. 2020). For example, Cunningham et al. demonstrated the use of Au–Ag NPs in a paper-based sensor for the electrochemical detection of AgNPs labels (Cunningham et al. 2016). Borah and Verbruggen utilized the alloys and core–shell arrangements for photothermal applications (Borah and Verbruggen 2020). Bijalwan et al. used the alloys coated on the sand for the reduction of the environmental pollutant 4-nitrophenol to 4-aminophenol (Bijalwan et al. 2020), Bai et al. studied the nanostructures for surface-enhanced resonance spectroscopy (Bai et al. 2015) and Shirman et al. studied methanol oxidation over nanoporous alloys (Shirman et al. 2018). The most studied applications of Au–Ag

NPs in nanomedicine engineering are the antibacterial effects due to the ability of the leached Ag ions to generate reactive oxygen species for killing bacteria (Chernousova and Epple 2013; Mijnendonckx et al. 2013; Loza et al. 2020).

Gold–silver nanostructures can be synthesized using immobilization by simple mixing of AuNPs and AgNPs, seeding by the chemical reduction of Ag over AuNPs, co-reduction by the chemical reduction of both Au(III) and Ag(I) salts, and galvanic exchange by mixing Au(III) with AgNPs (Sun and Xia 2004; Rioux and Meunier 2015; Panicker et al. 2020). On the other hand, the choice of the gold precursor is critical in the potential difference of the redox couple Au(III)/Ag(0) in the galvanic replacement. Furthermore, a few studies probed the mechanisms of the replacement reactions using Au in the oxidation states (I) and (III) (Sun et al. 2002; Sun and Xia 2004; Au et al. 2008; González et al. 2011; Wan et al. 2013; Bai et al. 2015; Jang and Min 2015; Rioux and Meunier 2015; Chen et al. 2016). The reduction of Au(I) compounds was reported at higher potentials than Au(III) (Mohamed et al. 1999, 2003). A comparative study involved $[AuCl_2]^-$ and $[AuCl_4]^-$ in the reaction with Au nanocubes (Au et al. 2008). In a related study, the galvanic exchange route was carried out via the reaction of $[AuBr_2]^-$ with citrate-capped AgNPs (Bai et al. 2015). Gold(III) was also used for galvanic exchange with Ag wires (Sun and Wang 2011).

Overall studies confirmed the role of the capping agents in gating the electron transfer at the surface (Zhang et al. 2011; Ma et al. 2012; Wu et al. 2013; Li et al. 2014; Long et al. 2017). Several techniques were used to probe Ag oxidation. Transmission electron microscopy, fluorescence electrochemical microscopy, single-particle hyperspectral images, X-ray photoelectron spectroscopy, and electrochemistry were used in probing the oxidative leaching, interfacial charge-transfer, and dynamic restructuring of Au–Ag NPs (Sun and Wang 2011; Nishimura et al. 2012; Toh et al. 2015; Holt et al. 2016; Plowman et al. 2016; Saw et al. 2016; Tanner et al. 2017a, b; Russo et al. 2018; Al-Zubeidi et al. 2021; Xie et al. 2021). Electrochemistry evolved as the first choice to relate the oxidation potential to the leaching of Ag in Au–Ag NPs drop-casted on the electrodes (Nishimura et al. 2012; Toh et al. 2015; Holt et al. 2016; Plowman et al. 2016; Saw et al. 2016; Tanner et al. 2017a, b; Russo et al. 2018).

Supporting electrolytes of KCl and KNO$_3$ were used in this study to control the solubility product which plays a major role in fine-tuning the redox behavior of Ag (Russo et al. 2018). The rich information gained on oxidative dissolution (dealloying) thus far by Compton, Merkoçi, and Tschulik in this research concludes with the facile control of Ag oxidation in Au–Ag NPs (Nishimura et al. 2012; Toh et al. 2015; Holt et al. 2016; Plowman et al. 2016; Saw et al. 2016; Tanner et al. 2017a, b; Russo et al. 2018).

Literature on the antibacterial effects of Ag is focused on several factors that control the structural development and release of Ag ions from Au–Ag alloy and core–shell nanostructures. The correlation of a few factors was reported such as the storage effect on the Ag ion release and toxicity mechanism, size effect on Ag ion release, electrolyte effect on the electrochemical oxidation of Ag, atomic structure effect on toxicity mechanism and antibacterial effect, organic surface ligand and antibacterial effect, size effect on the Ag ion release under neutral and acidic conditions, and thickness effect on the antibacterial properties (Martínez et al. 1993; Shibata et al. 2002; Pallavicini et al. 2010; Kittler et al. 2010; Liu et al. 2010, 2016; Das et al. 2012; Hahn et al. 2012; Peretyazhko et al. 2014; Gilroy et al. 2014; Ivask et al. 2014; Padmos et al. 2015; Yang et al. 2017; Bhattacharya et al. 2018; Ray et al. 2018; Zheng and Xie 2020; Dolinska et al. 2020).

This study aims to synthesize Au–Ag NPs using the galvanic replacement method and probe their electrochemical properties and relate them to the antibacterial effects. Diazonium gold(III) salts possess extremely low reduction potentials which makes them the first choice in redox chemistry in surface modification. We evaluated the antibacterial activity of Au–Ag NPs solutions prepared by the galvanic replacement on gram-positive *Staphylococcus aureus, Staphylococcus epidermidis, Enterococcus faecalis,* and gram-negative *Escherichia coli*, *Salmonella typhimurium,* and *Pseudomonas aeruginosa* ATCC strains. For the analysis of the antibacterial properties, the well diffusion and minimum inhibitory concentration, and minimum bactericidal concentrations were evaluated according to Clinical and Laboratory Standards Institute (CLSI) guidelines (Wikler 2006). The ability to inhibit

Staphylococcus epidermidis biofilm is evaluated by crystal violet assay.

Experimental and methods

Chemicals

Sodium nitrite, hydrochloric acid (36.5–38.0%), 4-aminobenzoic acid, polyvinylpyrrolidone (PVP), and ethyl acetate from Sigma-Aldrich. Potassium chloride from Riedel-de Haën and potassium nitrate from Merk Millipore. HAuCl$_4$ was synthesized in our laboratory from gold metal. Sodium borohydride from Fisher Chemicals. Silver nitrate from PanReac AppliChem. Crystal violet, nutrient agar, and Muller Hinton broth from HIMEDIA, India. *Staphylococcus aureus* ATCC 29213, *Staphylococcus epidermidis* ATCC 14990*, Enterococcus faecalis* ATCC 29212, *Escherichia coli* ATCC 25922, *Salmonella typhimurium* ATCC 29629, and *Pseudomonas aeruginosa* ATCC 27553 from American Type Culture Collection ATCC.

Instruments

The synthesized Au–Ag NPs were characterized with a high-resolution transmission electron microscope (HR-TEM, Field Emission JEM-2100F, JEOL, Japan). The composition of Au and Ag in the samples was determined with energy dispersive X-ray spectroscopy installed in HR-TEM. For the analysis, the nanoparticles in H$_2$O/ethyl ether were immobilized on a TEM grid of FORM-VAR FCF 400-Cu (Electron Microscopy Sciences, Hatfield, Pennsylvania, USA). The ImageJ software provided by the United States National Institutes of Health was used to measure lattice spacings and the sizes of the synthesized samples. UV–visible absorption spectra were measured using a scanning spectrophotometer (Spectro UV-2510TS, Labomed Inc.) in the 200–800 nm range with 2 nm resolution. X-ray powder diffraction (XRD) data were collected using Bruker D8 ADVANCE diffractometer with Cu-Kα X-ray source at λ = 1.5406 Å operating at 40 kV tube voltage and 40 mA current. Dynamic light scattering (DLS) measurements and ζ-potential analysis

of the synthesized nanoparticles in water were carried out using Anton Paar Litesizer 500 and analyzed using KalliopeTM software. A Renishaw Ramascope was used for Raman measurements at a laser excitation wavelength of 785 nm in the scale range 200–3000 cm^{-1}.

Cyclic voltammetry (CV) studies were performed using CH Instrument electrochemical analyzer Model 660. The electrochemical cell is comprised of glassy carbon (GC) electrode, Pt wire counter electrode, and a saturated calomel electrode (SCE) reference electrode, known as a three-electrode setup, was employed for the analysis. For cyclic voltammetry measurements, the GC working electrode was polished with 0.05 μm Buehler micro polish alumina powder, washed with deionized water, sonicated for 5 min, and dried with acetone. Before the electrochemical measurements, the solutions in 20 mM KCl or KNO$_3$ supporting electrolytes were bubbled for 10 min and were blanketed with nitrogen gas while conducting the experiments. Background cyclic voltammograms were acquired before the drop-casting. Potentials are reported versus SCE reference electrode at room temperature and are not corrected for liquid junction potentials.

Dissolved silver concentrations were determined using simultaneous ICP-OES (inductively coupled plasma-optical emission spectroscopy-ICP-Varian, Vista MPX CCD model).

Synthesis of AgNPs-PVP

AgNPs-PVP samples were synthesized using a modified procedure (Panicker et al. 2020). Briefly, 20 mL of 80 mM NaBH$_4$ was taken in an Erlenmeyer flask and placed in an ice bath under stirring. The solution was kept under stirring for 30 min, and then 5 mL of 1% PVP and 1.0 mM AgNO$_3$ solution was added dropwise simultaneously into the stirring NaBH$_4$ solution. Stirring was stopped as soon as all AgNO$_3$ was added and a clear yellowish-brown solution of AgNPs-PVP was formed. The solution was heated at 40 °C for 3 h to remove the excess NaBH$_4$ and filtered using cellulose tape. The solution was kept at 4 °C in the fridge for further use.

Synthesis of [HOOC-4–C$_6$H$_4$N≡N]AuCl$_4$

Aryldiazonium tetrachloroaurate(III) salt was synthesized according to our previously published procedure (Ahmad et al. 2019). The 4-aminobenzoic acid of 3.0 mM was dissolved in 6 M HCl and 4.5 mM sodium nitrite was dissolved in 5.0 mL of DI water. Both solutions were mixed at 0.0–5.0 °C and stirred for 1 h. Tetrachloroauric(III) acid of 3.0 mM was dissolved in DI water and added slowly to the mixture. The obtained yellow precipitate was filtered and washed for further use.

Preparation of Au–Ag NPs

To the pre-synthesized AgNPs-PVP, 1 mM aqueous solution of aryldiazonium gold(III) salt was suspended and was allowed to exchange overnight undisturbed at room temperature. AgNPs reduced the aryldiazonium salt and a reddish-blue Au–Ag NPs solution was formed. Similarly, another set of 5 mM and 10 mM aryldiazonium gold(III) solutions were also mixed with AgNPs-PVP solution and stirred overnight.

Oxidative leaching measurement of silver

Leaching studies were performed on AgNPs-PVP and Au$_{0.91}$Ag$_{0.09}$ and Au$_{0.79}$Ag$_{0.21}$ NPs in water. One mL of 1 M NaCl was added to 2 mL each of both solutions. They were mixed and incubated at room temperature for 1 h. UV–visible spectra were recorded after 1 h.

Electrochemical study

Cyclic voltammetry (CV) measurements were done by loading samples on glassy carbon (GC) working electrodes with the drop-casting method. A glassy carbon disk electrode with a diameter of 3 mm was used. Before loading, the GC electrode surface was cleaned with DI water, ethanol, and acetone. Then, 5 μL of the sample dispersion was transferred onto a glassy carbon electrode and dried in the open air. Cyclic voltammogram of samples including AgNPs-PVP, Au$_{0.91}$Ag$_{0.09}$, and Au$_{0.79}$Ag$_{0.21}$ were drop casted on glassy carbon electrode in 20.0 mM KCl or 20.0 mM KNO$_3$ at 50 mV/s scan rate.

Antibacterial activities

Well diffusion method

Antibacterial activities of the nanoparticles were evaluated with the well diffusion method on six strains: three gram-positive *Staphylococcus aureus* ATCC 29213, *Staphylococcus epidermidis* ATCC 14990*,* and *Enterococcus faecalis* ATCC 29212, and three gram-negative *Escherichia coli* ATCC 25922, *Salmonella typhimurium* ATCC 29629, and *Pseudomonas aeruginosa* ATCC 27553. The direct colony suspension method was used to prepare the standard inoculums from 24 h agar culture plates. The inoculum optical density was adjusted to 0.5 McFarland standard at 600 nm using DensiCHEK™ to give a concentration of 1×10^8 CFU mL^{-1}. Then, it was spread over Muller Hinton agar surface with a cotton swab. Then, wells with a diameter of 7 mm were punched, and 50 μL of the samples were introduced into the wells. Then, agar plates were incubated at 37 °C overnight. The zone of inhibition was measured in mm. Erythromycin of 15 μg was used as a control for the gram-positive and gentamicin 50 μg for gram-negative bacteria.

Micro-broth dilution method

The micro-broth dilution method was used to determine the Minimum Inhibitory Concentrations (MIC) and Minimum Bactericidal Concentrations (MBC) according to the Clinical and Laboratory Standards Institute (CLSI) (Wikler 2006). Briefly, the testing solutions were double diluted in Muller Hinton broth. Standard bacterial inoculums were tested at a final concentration of 5×10^5 CFU mL^{-1} in 100 μL of the testing solution. Control wells of broth with bacteria and sterile wells containing broth only were set. Plates were sealed and incubated overnight in a shaking incubator at 37 °C. MIC was detected visually. Minimum concentrations that kill 99.9% of the initial inoculum were detected by sub-culturing 10 μL of the samples from all wells that showed inhibition onto nutrient agar and incubated for 24 h at 37 °C, and the number of colonies was counted to find the MBCs. The MIC and MBC values were presented as dilution %.

In vitro biofilm formation assay

Microtiter Dish Biofilm Formation Assay was used to assess the inhibition of *Staphylococcus epidermidis* biofilm formation and was evaluated by the crystal violet method. In brief, 200 μL of Tryptic Soy Broth (TSB) broth containing 10^5 CFU mL^{-1} along with MIC, 2 MIC, and 1/2 MIC of Au–Ag NPs were inoculated in sterile 96 wells of polystyrene microtiter plate. The plate was incubated in a static mode at 37 °C for 48 h. The negative and positive control wells maintained the absence of nanoparticles and sterility wells as a negative control. After the formation of the biofilm, the content of each well was removed, washed twice with sterile normal saline, stained with 200 μL of 0.1% w/v crystal violet solution, and incubated for 30 min at room temperature. Thereafter, the excess solution was removed, and the plate was washed twice with normal saline and air-dried. The bound stain was solubilized using 200 μL of 95% ethanol and the optical density (OD) was scanned at 590 nm. The amount of biofilm inhibition was calculated relative to the amount of biofilm that was grown in the absence of nanoparticles (defined as 100% biofilm) and the media sterility control (defined as 0% biofilm).

Statistical analysis

Statistical analysis was performed using paired Student t test, P values of 0.05 were considered significant. Single stars denote $0.01 < P < 0.05$, double stars $0.001 < P < 0.01$, and triple stars $P < 0.001$.

Results and discussion

Synthesis and characterization

Au–Ag NPs were synthesized using galvanic exchange of AgNPs-PVP with aryldiazonium gold salt [HOOC-4-C$_6$H$_4$N≡N]AuCl$_4$ in different ratios at room temperature in water, Fig. 1A. Diazonium salts of 1 mM and 5 mM were successfully reduced using AgNPs-PVP. Figure 1B shows UV–visible spectra of the plasmon peaks of the parent AgNPs-PVP at 400 nm and Au–Ag NPs at 544 nm. Figure 1C displays the cuvettes of AgNPs and Au–Ag NPs. The formation of Au–Ag NPs was monitored with time as
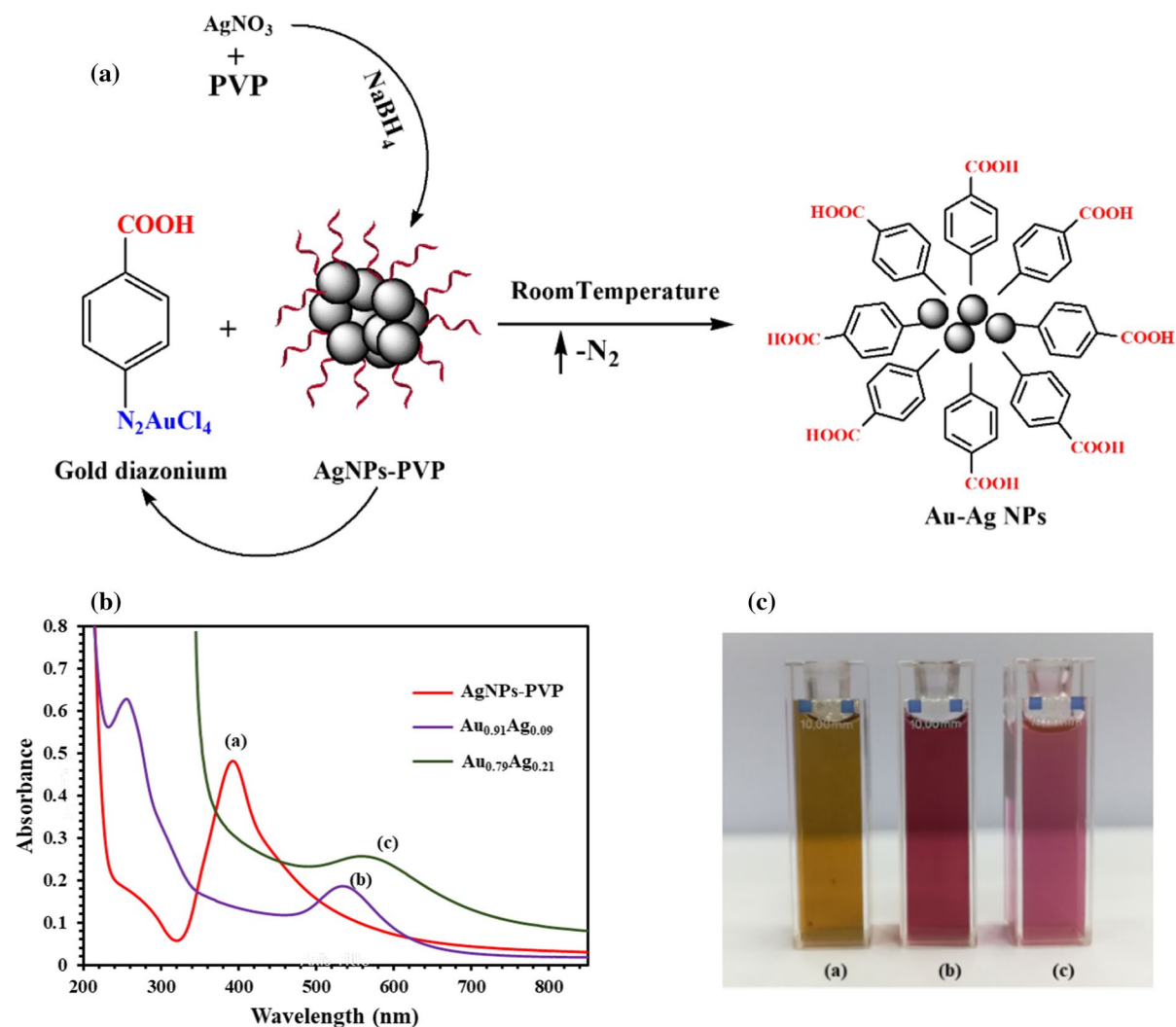
Fig. 1 A Schematic representation of the synthesis of Au–Ag NPs from aryldiazonium gold(III) salts, **B** UV–visible spectra of (a) AgNPs, (b) $Au_{0.91}Ag_{0.09}$, and (c) $Au_{0.79}Ag_{0.21}$ (y-axis shown in Fig. 2a, b. Silver plasmon peak at 400 nm disappeared upon the addition of the diazonium salt and the Au plasmon peak at 544 nm started to grow with time, Fig. 2.

not to scale), and **C** cuvette images showing the colors of (a) AgNPs-PVP, (b) $Au_{0.91}Ag_{0.09}$, and (c) $Au_{0.79}Ag_{0.21}$

The effect of diazonium salt concentration on the exchange reaction was monitored and we were able to successfully exchange Au(III) to Au(0) using AgNPs at low concentrations of diazonium such as 1 mM and 5 mM termed as $Au_{0.91}Ag_{0.09}$ and $Au_{0.79}Ag_{0.21}$, respectively according to the elemental composition obtained from EDS installed in TEM. But when the concentration of the diazonium salt increased to

10 mM (equimolar Au and Ag), the solution became white cloudy and a precipitate was settled over time, apparently AgCl. This indicates that the effect of diazonium concentration is crucial with an optimum Au:Ag ratio for the successful fabrication of Au–Ag NPs. Increased diazonium concentration corresponds to the concentration ratios of 1:10 (Au–Ag) and 1:5 (Au–Ag) for $Au_{0.91}Ag_{0.09}$ and $Au_{0.79}Ag_{0.21}$, respectively. When we increased the diazonium concentration further to 1:1 (Au:Ag) there may not be sufficient Ag(0) to completely reduce Au(III) to Au(0). Also, generated Ag(I) ions may easily react with chloride
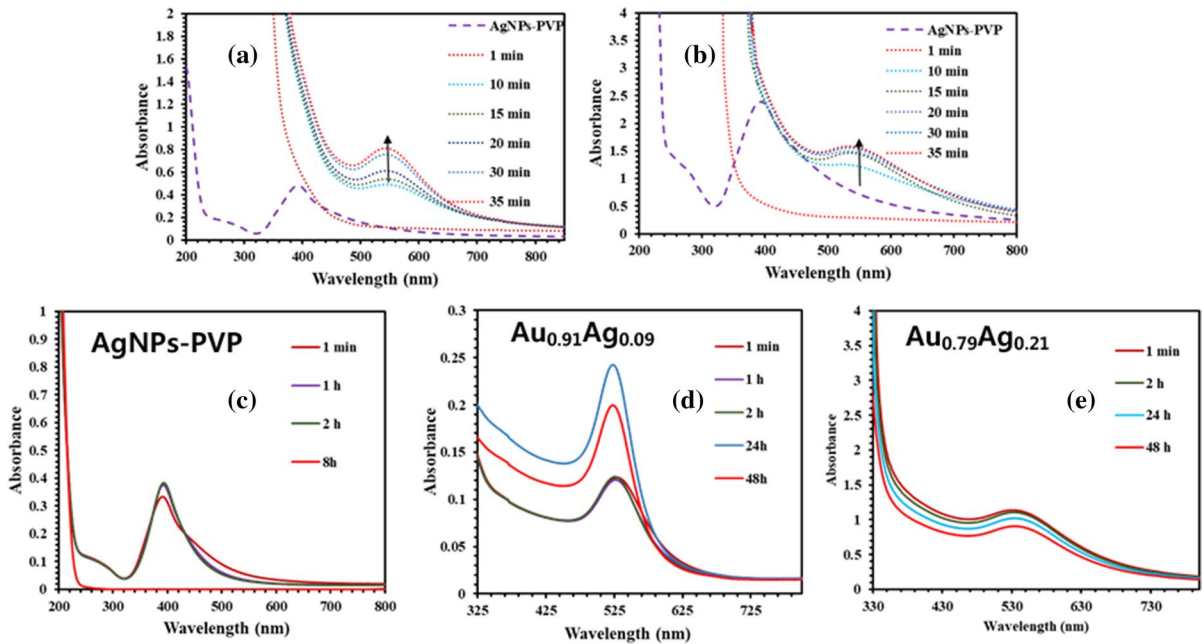
Fig. 2 UV–visible spectra for the formation of the peak with the time of **a** $Au_{0.91}Ag_{0.09}$ and **b** $Au_{0.79}Ag_{0.21}$. Leaching studies in 1 M NaCl of **c** AgNPs-PVP, **d** $Au_{0.91}Ag_{0.09}$, and **e** $Au_{0.79}Ag_{0.21}$

Table 1 Particle size and zeta potential measurements in water

	Hydrodynamic diameter (nm)	Zeta potential (mV)
AgNPs-PVP	12.9	− 14.98
$Au_{0.91}Ag_{0.09}$	46.4	− 44.56
$Au_{0.79}Ag_{0.21}$	74.8	− 25.09

ions from excess diazonium tends to produce insoluble AgCl. It was also observed that the amount of Ag in $Au_{0.91}Ag_{0.09}$ and $Au_{0.79}Ag_{0.21}$ NPs was diametrically the opposite to the amount of Ag precursor added in the synthesis solution, Eq. (1).

$$4Ag\,(s) + diazonium\,[AuCl_4]\,(aq) \rightarrow Au(aryl)_n(s)$$
$$+ 4Ag^+(aq) + 4Cl^-(aq)$$
$$(1)$$
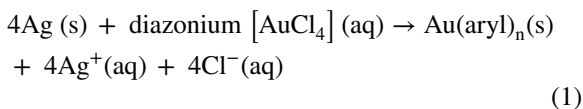
The leaching of Ag ions from AgNPs-PVP and Au–Ag NPs was studied using 1 M NaCl. Both solutions were mixed with 1 mL of 1 M NaCl and incubated at room temperature for 1 h before UV–visible spectra were recorded. The plasmon peak of AgNPs-PVP showed a significant decrease after 8 h of mixing indicating complete leaching of AgNPs, however,

Au–Ag NPs showed no leaching within the same time range, Fig. 2c–e. However, slight leaching was observed for Au–Ag NPs plasmon peak after 24 h.

Hydrodynamic sizes and surface charges of the materials in water were probed using dynamic light scattering and zeta potential (ζ-potential), Table 1. The average hydrodynamic size of AgNPs-PVP increased from 12.9 nm to 46.3 nm and 74.8 nm, respectively (See Fig. S1). Corresponding polydispersity index (PDI) values obtained from DLS for AgNPs-PVP, $Au_{0.91}Ag_{0.09}$ and $Au_{0.79}Ag_{0.21}$ NPs are 0.36 (36.2%), 0.35 (35.5%) and 23.2 (23.2%), which indicate their quality with respect to the size distribution. The measured ζ-potential of AgNPs-PVP in water was − 14.98 mV, arising generally from the PVP functionalities. The results showed that $Au_{0.91}Ag_{0.09}$ and $Au_{0.79}Ag_{0.21}$ NPs have ζ-potential values of − 44.56 mV and − 25.09 mV. The increased particle size with a high concentration of Au in Au–Ag ratio was also observed in TEM images (vide infra). The nanoparticles were further analyzed using powder X-ray diffraction (PXRD) (See Fig. S2). The observed characteristic peaks for face-centered cubic (fcc) AuNPs reflections (PDF Card #4-784) are $2\theta = 38.1°, 44.1°, 64.5°, 77.5°$, and $81.5°$.

Raman spectroscopy revealed Au–Ag NPs with aryl organic shells -4-C_6H_4-COOH. For instance, the bands at 666 and 1053 cm^{-1} are assigned to ring deformations (Kwon et al. 1994). Characteristic peaks like δ_{COO} at 850 cm^{-1} and 1610 cm^{-1} are assigned to C=O functional group arising from carboxylic indicates the presence of the aryl shell (See Fig. S3) (Pagannone et al. 1987; Yu et al. 2001). Moreover, the diazonium peak disappearance at 2270 cm^{-1} supports the complete reduction of the salt. Also, there is a significant enhancement of the signal at 2945 cm^{-1} (ν_{as} of CH_2 in the skeletal chain of PVP) compared with AgNPs-PVP which reveals that the CH_2 chain is close to the surface of AuNPs (Mao et al. 2012).
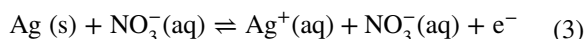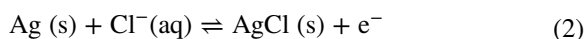
The Au–Ag NPs with different amounts of Au precursors are mostly spherical, Fig. 3 ($Au_{0.91}Ag_{0.09}$) and Fig. 4 ($Au_{0.79}Ag_{0.21}$). The nanoparticles were completely crystallized as confirmed by the observation of sample lattice spacings. As shown in Fig. 3d, the measured lattice spacings of $Au_{0.91}Ag_{0.09}$ of 0.195 nm and 0.200 nm corresponding to the (200) plane of Au, confirmed the formation of metallic Au. Interestingly, in the sample synthesized with more Ag precursor, three lattice spacings of 0.198 nm, 0.24 nm, and 0.144 nm were measured, respectively corresponding to (200), (111), and (220) planes of Au. Also, 0.240 nm and 0.198 nm of the measured lattice spacings in the $Au_{0.79}Ag_{0.21}$ sample may correspond to (111) and (200) planes of Ag. Berahim et al. reported similar results that two different lattice spacings of 0.20 nm for (200) plane of Ag and 0.24 nm for (111) plane of Au were observed when the bimetallic Au–Ag NPs were synthesized (Berahim et al. 2018). This result strongly proved the successful formation of Au–Ag NPs for both samples. Our previous studies also reported that the lattice spacing of 0.235 nm, corresponding to the (111) plane of Au or Ag, was observed in the prepared Au–Ag NPs with a green synthesis method (Han et al. 2014, 2015).

As shown in Fig. 3e, the atomic weight% of Au and Ag were 91.2% and 8.8%, respectively, confirming the presence of both Au and Ag in Au–Ag NPs sample. The synthesized nanoparticles ranged from 4.6 to 33.3 nm and the average size was 12.8 ± 4.9 nm, Fig. 3 and Table S1. As shown in Fig. 4e, the atomic weight% of Au and Ag were 78.7% and 21.3%, respectively, confirming the presence of both Au and Ag in Au–Ag NPs sample. The synthesized

nanoparticles ranged from 7.9 to 56.5 nm and the average size was 25.6 ± 14.4 nm, Fig. 4 and Table S2. The content of Ag in Au–Ag NPs was the opposite of the amount of Ag precursor used and particle sizes of the samples also increased at high concentrations of Au in Au–Ag ratio.

Electrochemistry

Cyclic voltammetry studies were performed in 20 mM KCl and KNO_3 supporting electrolytes to investigate the oxidation behavior of Au–Ag NPs, as the results provide insights into the stability of the alloys and the rate of Ag oxidative release in antimicrobial media. First, the CV of pure AgNPs-PVP was studied on AgNPs drop-casted glassy carbon electrodes vs SCE, Fig. 5a, b. Here, an oxidative peak is observed at 0.16 V in KCl (Fig. 5) and 0.33 V in KNO_3 (data not shown). The potential values are in agreement with literature work and assigned to AgNPs oxidation to ionic Ag, Eqs. (2) and (3) (Plowman et al. 2016).

$$Ag\ (s) + Cl^-(aq) \rightleftharpoons AgCl\ (s) + e^- \qquad (2)$$

$$Ag\ (s) + NO_3^-(aq) \rightleftharpoons Ag^+(aq) + NO_3^-(aq) + e^- \qquad (3)$$

Second, the CV of Au–Ag NPs was studied as shown in Fig. 5c–f. For the $Au_{0.91}Ag_{0.09}$ sample, oxidative peaks are observed in the forward scans at 0.16 V and 1.4 V for Ag and Au respectively and traces of AgCl reduction in the reverse scan. From Fig. 5d, we can see the magnitude of the Ag oxidation peak increased when compared with AgNPs-PVP, and the Au oxidation is diminished after the first cycle. Similarly, oxidative peaks in the forward scans for $Au_{0.79}Ag_{0.21}$ samples are also the same, however, the magnitude of Ag oxidation is considerably less than $Au_{0.91}Ag_{0.09}$. The complexing chloride ion enhances the dissolution of Ag to form AgCl which is thermodynamically favored. The low oxidation potential in KCl electrolyte could be explained based on the tendency to form AgCl away from the electrode and becomes hard to bring back to reduce on the electrode in the reverse scans. Our interpretation is supported by the absence or the small peak presence on the reverse scan due to
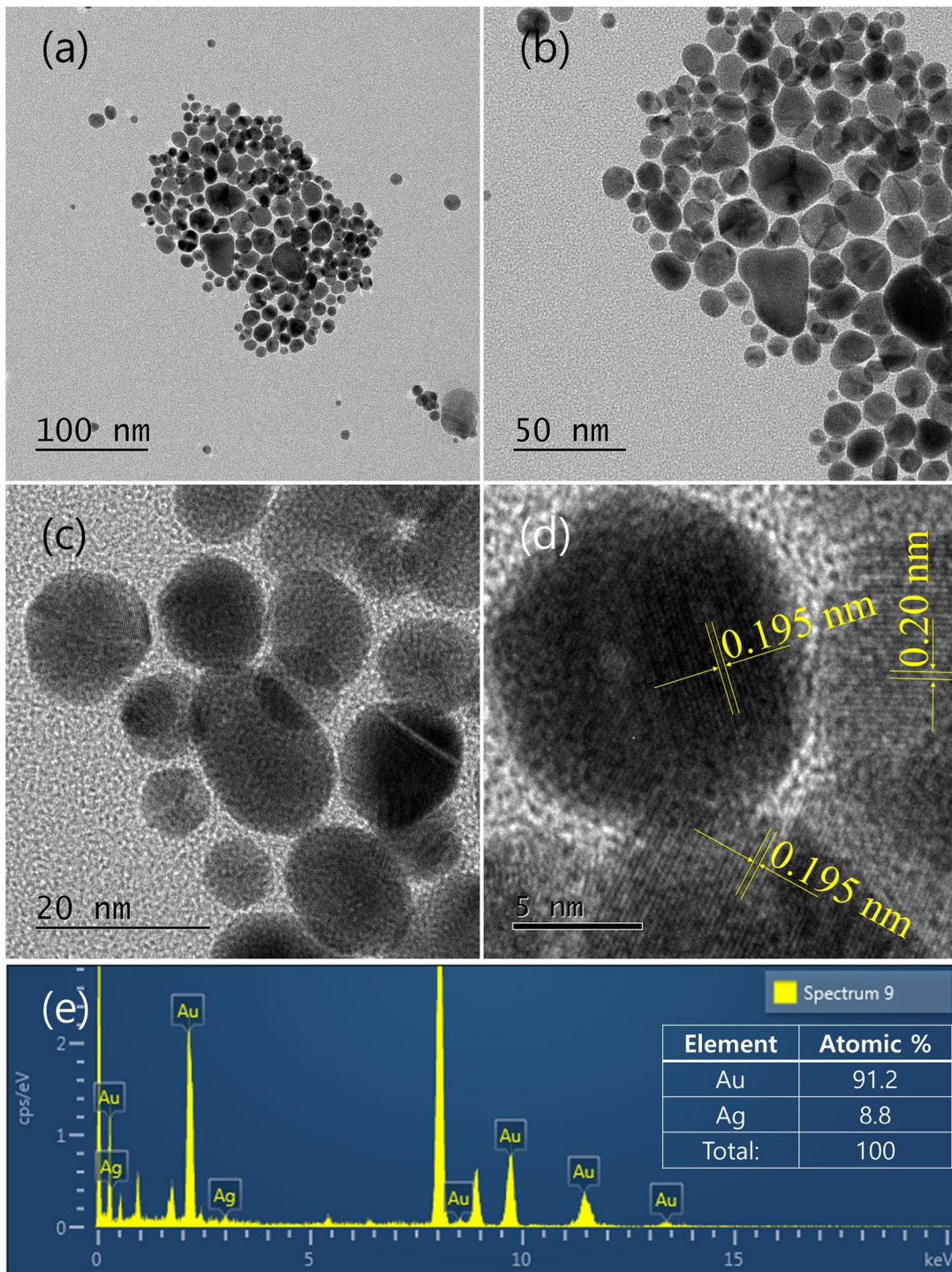
Fig. 3 **a–c** TEM, **d** HR-TEM images, and **e** EDS spectrum of $Au_{0.91}Ag_{0.09}$ sample

AgCl reduction at low potential. The reduction peak is greatly attenuated at the second and third scans.

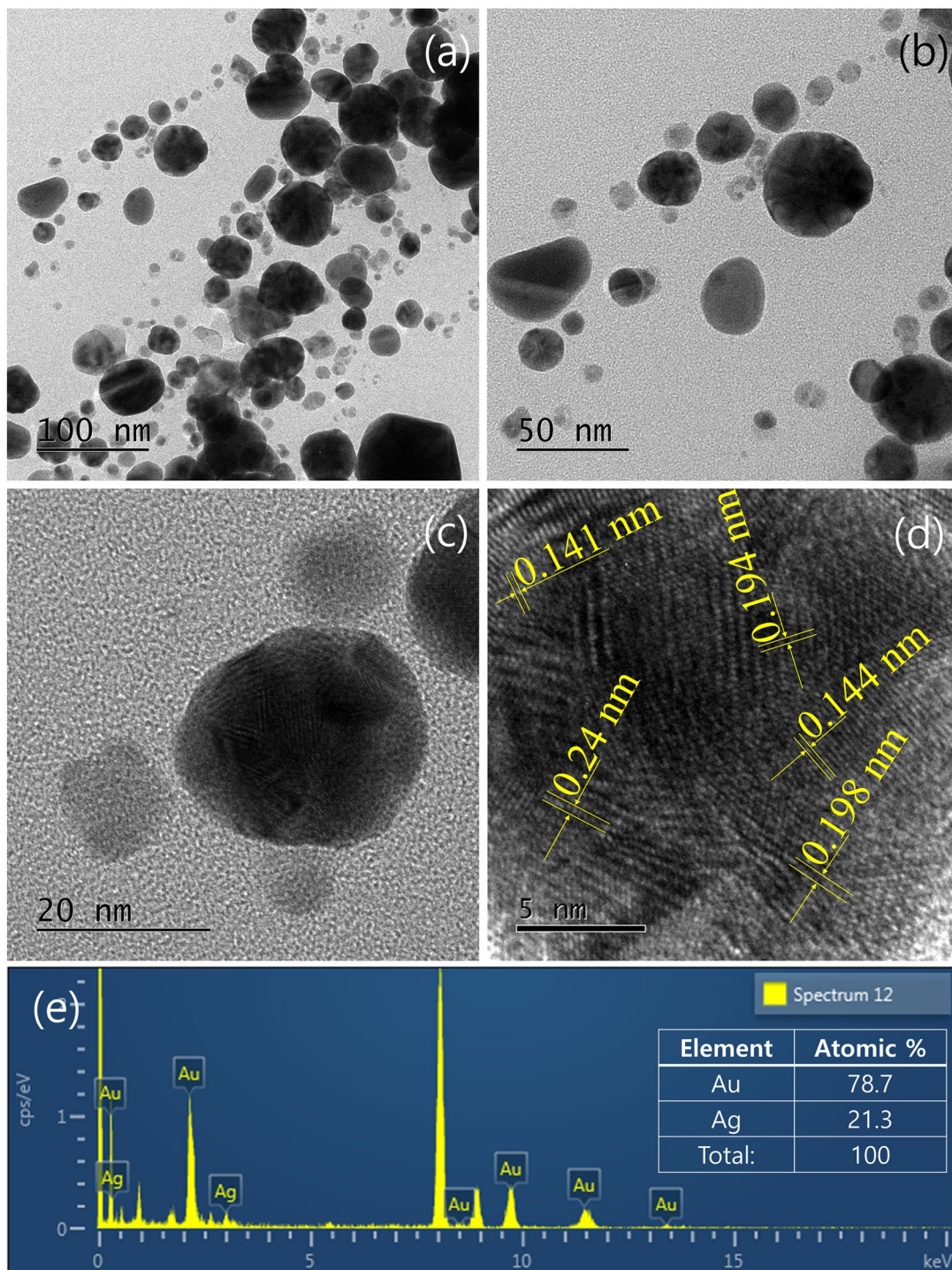Continuous dissolution probably occurred from the first cycle to the consecutive cycles in the case of

Fig. 4 **a–c** TEM, **d** HR-TEM images, and **e** EDS spectrum of $Au_{0.79}Ag_{0.21}$ sample
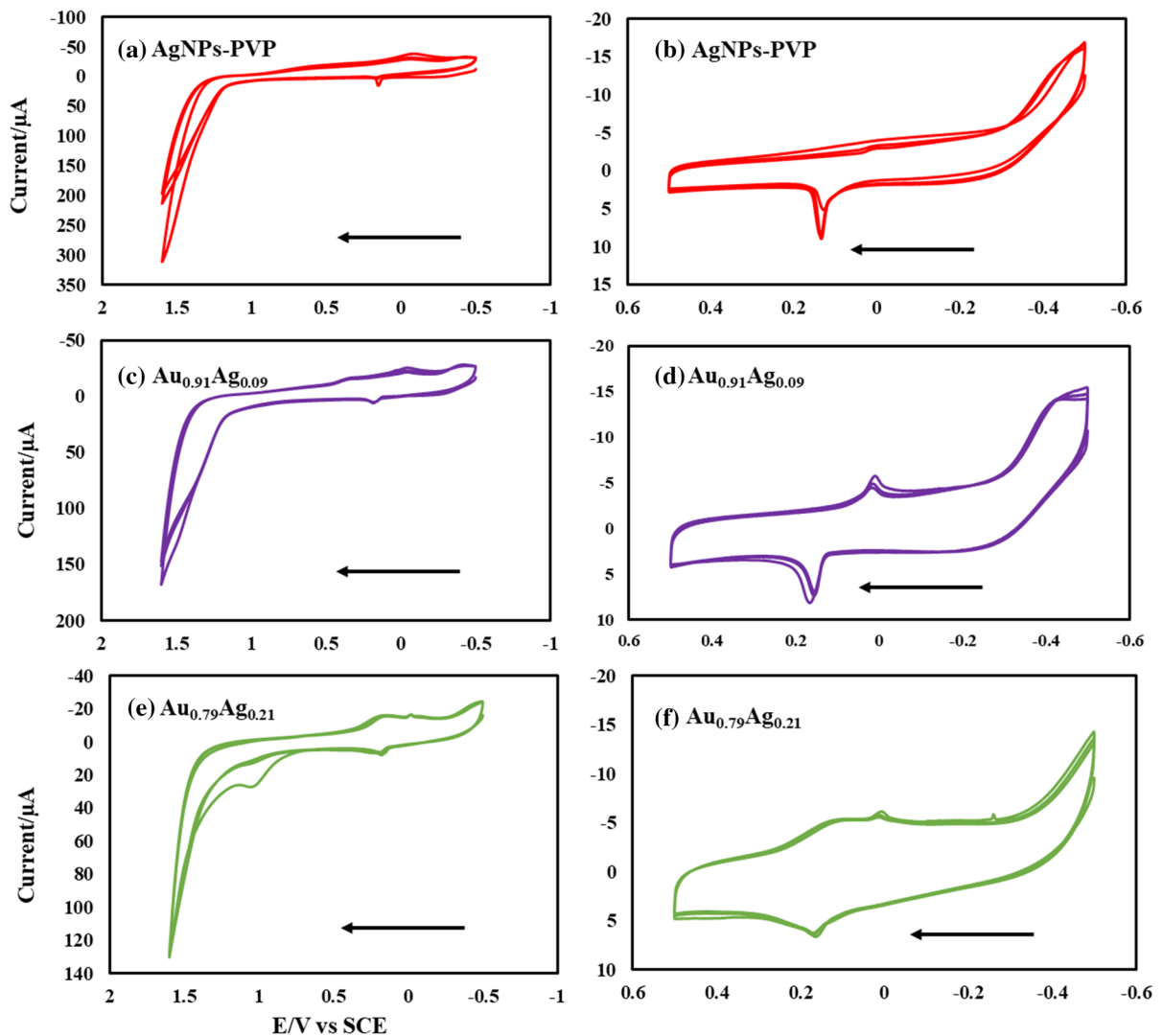
Fig. 5 Cyclic voltammograms of 5 µL nanoparticles drop-casted on GC electrodes in 20 mM KCl vs. SCE at 50 mV/s scan rate for **a** AgNPs-PVP: − 0.5 to +1.6 V range, **b** AgNPs-PVP: − 0.5 to +0.5 V range, **c** $Au_{0.91}Ag_{0.09}$ − 0.5 to +1.6 V range, **d** $Au_{0.91}Ag_{0.09}$: − 0.5 to +0.5 V range, **e** $Au_{0.79}Ag_{0.21}$: − 0.5 to +1.6 V range, and **f** $Au_{0.79}Ag_{0.21}$: − 0.5 to +0.5 V range

AgNPs-PVP. On the other hand, the oxidation of Ag over the next few cycles behaved differently in the presence of Au. The oxidation of Ag in the alloys is very slow and far from quantitative.

Following the same procedure of electrochemistry in 29 mM KCl, we also looked at the electrochemical behavior of Ag in the alloys in the presence of the non-complexing supporting electrolyte KNO_3, Eq. (3). The electrochemistry results of AgNPs behaved slightly differently and the oxidation peak is prominent and shifted to higher potential, i.e., 0.4 V

vs. SCE. In addition, the reduction peak of Ag possesses more current on the reverse scan. This could be due to the free Ag cations in the solution available for the electrochemical reduction on the electrode surface. The Au–Ag NPs also showed lower oxidation potential values compared with AgNPs, however, higher than the potential values in KCl. The comparison studies support the facile removal of Ag from the alloys in the presence of chloride compared with KNO_3 because of the formation of AgCl. Overall results are supported by the literature investigation

Table 2 Zone of inhibition in mm for Au$_{0.91}$Ag$_{0.09}$, Au$_{0.79}$Ag$_{0.21}$, and AgNPs-PVP

Bacteria ATCC	Zone of inhibition (mm $\pm$ SD)			
	Au$_{0.91}$Ag$_{0.09}$	Au$_{0.79}$Ag$_{0.21}$	AgNPs-PVP	Control
S. aureus 29213	19.0 ± 0.6	16.0 ± 0.6	–*	23.0 ± 0.6
S. epidermidis 14990	15.0 ± 0.6	13.0 ± 0.6	–	25.0 ± 0.6
E. faecalis 29212	18.0 ± 0.6	10.0 ± 1.0	–	22.0 ± 1.0
E. coli 25922	12.0 ± 0.6	10.0 ± 1.0	–	20.0 ± 0.6
S. typhimurium 29629	24.0 ± 1.0	14.0 ± 1.0	–	21.0 ± 0.6
P. aeruginosa 27553	13.0 ± 0.6	12.0 ± 0.6	–	20.0 ± 1.0

Erythromycin of 15 μg was used as a control for the gram-positive and gentamicin 50 μg for the gram-negative bacteria

*No activities

on AgNPs and Au–Ag NPs in chloride and nitrate supporting electrolytes (Nishimura et al. 2012; Toh et al. 2015; Holt et al. 2016; Plowman et al. 2016; Saw et al. 2016; Tanner et al. 2017a, b; Russo et al. 2018; Xie et al. 2022). We can extract the fact that AgCl is thermodynamically favored over AgSCN and AgNO$_3$. For example, the poorly soluble AgCl has K$_{sp}$ of 1.8×10^{-10} compared with the highly soluble AgNO$_3$ of K$_{sp}$ = 51.6 at 25 °C. Nevertheless, to confirm the hypothesis of the effect of electrolytes, the oxidative removal of Ag from drop-casted GC electrodes occurred and is dependent on the electrolyte.

It is worth adding comments on the electrochemical results of Au in the alloys. Figure 5c and e show the oxidation peaks of Au in Au$_{0.91}$Ag$_{0.09}$ and Au$_{0.79}$Ag$_{0.21}$ NPs samples, respectively. Gold showed a small oxidation peak in the two alloys due to the formation of tetrachloroaurate(III), Eq. (4). A considerable enhancement in the Au oxidation occurred in the low Au ratio alloy, Au$_{0.79}$Ag$_{0.21}$. The pronounced Au oxidation peak in low Au ratio alloy could be due to the electron depletion of Au by Ag which facilitated the loss of electrons (Nishimura et al. 2012). Hence, the chemical stability of Au–Ag NPs to the charge transfer from Au to Ag which in turn can modify the electronic structures. Gold oxidation occurred in the chloride-rich electrolyte compared with those almost nonexistent in KNO$_3$. In chloride electrolyte, the oxidation potential at 1.1 V vs SCE is clear however almost disappeared in the next few cycles.

$$Au\ (s)\ +\ 4Cl^-(aq) \rightarrow \left[AuCl_4\right]^-(aq) \quad (4)$$

To this end, the literature presented a few examples of electrochemistry of Ag oxidation controlled by a few factors such as size, medium, coordinating anion, and capping agent. Meanwhile, the PVP capping agent is critical in controlling the oxidation of AgNPs. Compton results support our conclusion that PVP decreased the oxidation potential of Ag in its alloys compared with several capping agents (Toh et al. 2015; Tanner et al. 2017a, b). Another trial we attempted is the electrochemical studies in solution versus drop-casted on GC electrode. We have drawn a clear insight that solution studies resulted in inconsistent and very attenuated oxidation peaks due to blocking the electrode among other factors. Zamborini studied the effect of electrode material grafting methods such as electrostatic attachment, electrophoretic deposition, and drop-casting deposition on the electrochemical oxidation of AuNPs (Pattadar et al. 2019). The E$_{ox}$ value and aggregation state can be greatly affected by the solution versus drop-casted samples as electrodes for electrochemical studies as it is clear from our investigation. Hence, casting electrodes could be the best method to probe the electrochemical oxidation of AgNPs and Au–Ag NPs.

Antibacterial susceptibility

Controlling the release of Ag cation because of its oxidation in biological media can be beneficial for the long-term use of Au–Ag NPs in antibacterial substrates. Physicochemical properties can affect the release of Ag, hence each group of AgNPs and their alloys must be evaluated independently. Here, we study the alloys synthesized in this work for antibacterial efficacy. From CV results, we can conclude that Au$_{0.91}$Ag$_{0.09}$ of less Ag ratio is prone to oxidative leachability. Moreover, this supports the dissolution of Ag cation as the most acceptable mechanism for the generation of reactive oxygen species for killing bacteria. To confirm our correlation, we carried out a
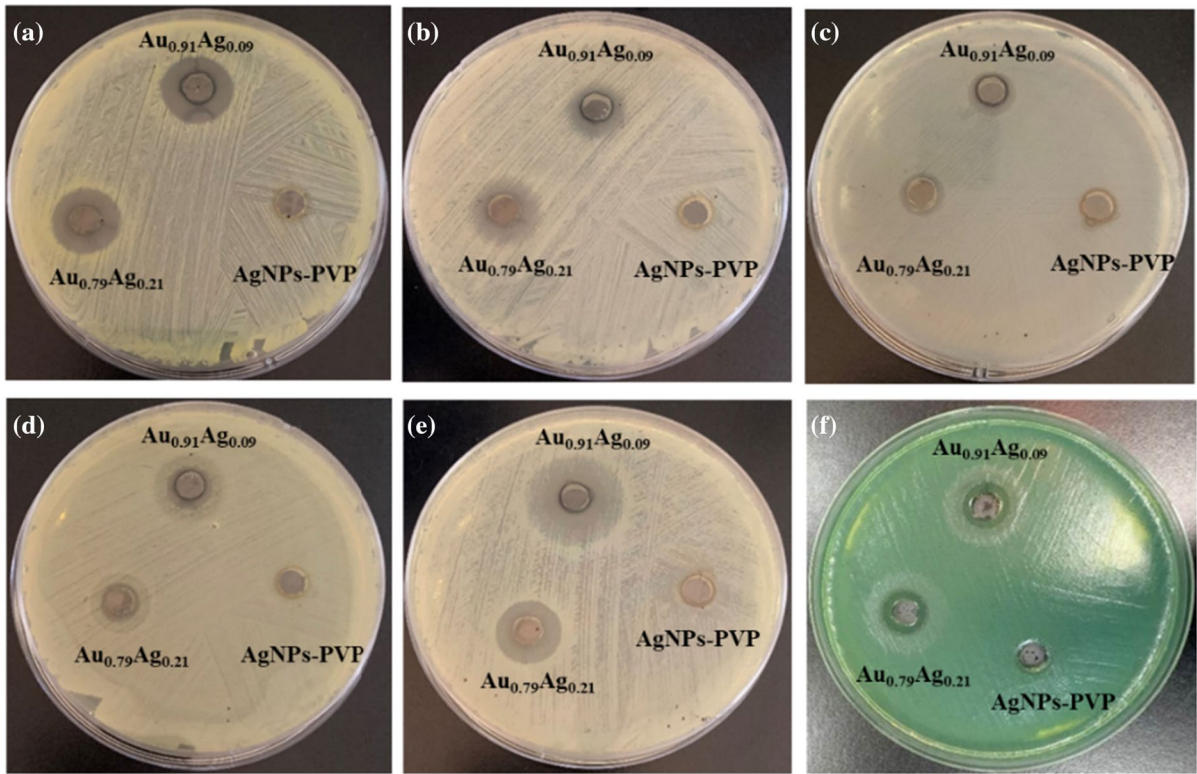
Fig. 6 Antibacterial susceptibility test, well diffusion method zone of inhibition for $Au_{0.91}Ag_{0.09}$, $Au_{0.79}Ag_{0.21}$, and AgNPs-PVP against **a** *S. aureus,* **b** *S. epidermidis,* **c** *E. faecalis,* **d** *E.* *coli,* **e** *S. typhimurium,* and **f** *P. aeruginosa* showing the inhibition with $Au_{0.91}Ag_{0.09}$ and $Au_{0.79}Ag_{0.21}$ but not with AgNPs-PVP

Table 3 MIC and MBC concentrations of $Au_{0.91}Ag_{0.09}$, $Au_{0.79}Ag_{0.21}$, and AgNPs-PVP

Bacteria ATCC	MIC (%)			MBC (%)		
	$Au_{0.91}Ag_{0.09}$	$Au_{0.79}Ag_{0.21}$	AgNPs-PVP	$Au_{0.91}Ag_{0.09}$	$Au_{0.79}Ag_{0.21}$	AgNPs-PVP
S. aureus 29213	3.125	25	–	3.125	25	–
S. epidermidis 14990	6.25	12.5	50	12.5	25	50
E. faecalis 29212	12.5	25	–	25	50	–
E. coli 25922	3.125	12.5	–	12.5	12.5	–
S. typhimurium 29629	3.125	25	–	3.124	25	–
P. aeruginosa 27553	12.5	25	–	12.5	25	–

few antibacterial studies. In addition, MIC and MBC values were also estimated.

Well diffusion method

Antibacterial susceptibility testing by well diffusion method was performed on ATCC strains, gram-positive *S. aureus* ATCC 29213, *S. epidermidis* ATCC 14990, *E. faecalis* ATCC 29212, and three gram-negative *E. coli* ATCC 25922, *S. typhimurium* ATCC 29629, and *P. aeruginosa* ATCC 27553 on Muller Hinton agar. Results showed an effective inhibition zone between 10.0 to 24.0 mm, Table 2. This finding suggests that both Au–Ag NPs have antibacterial activities on all tested strains, while no activity was demonstrated for AgNPs-PVP, Fig. 6.

Minimum inhibitory concentrations and minimum bactericidal concentrations

The micro-broth dilution method was used to determine the MIC and MBC following the CLSI guidelines, Table 3 (Wikler 2006). The Au–Ag NPs synthesized by galvanic replacement reaction demonstrated antibacterial activities towards all tested strains while AgNPs-PVP inhibited only *S. epidermidis* at 50% dilution, however, gold-aryl NPs did not show any activities on both strains as we reported in our previous study (Panicker et al. 2020). Galvanic Au–Ag NPs inhibited all strains. Our results indicate that the combination of Ag and Au enhanced the antibacterial activities of Ag more than the native AgNPs and AuNPs.

Further, silver ion concentrations in solutions can confirm the role of leached Ag in the antibacterial activity of both Au–Ag NPs. Inductively coupled plasma-optical emission spectroscopy was used to determine the concentration of dissolved Ag using Ag standard solutions of 2.94, 1.47, 0.73, 0.36, and 0.18 mM freshly prepared by dissolving $AgNO_3$ in deionized (DI) water to construct a calibration curve. A 500 μL volume of $Au_{0.91}Ag_{0.09}$, $Au_{0.79}Ag_{0.21}$, and AgNPs-PVP was mixed with Muller Hinton broth medium and was incubated overnight in a shaking incubator at 37 °C to create similar conditions to the antibacterial study. Further, the mixture was centrifuged at 5000 rpm for 20 min, and the supernatant and residues were separated. Supernatants were analyzed using ICP-OES. Silver ion concentrations of 1.1×10^{-2} mM for $Au_{0.91}Ag_{0.09}$ and 4×10^{-3} mM for $Au_{0.79}Ag_{0.21}$ and AgNPs-PVP were determined. This supports that the dissolution of Ag is more prominent in $Au_{0.91}Ag_{0.09}$ relative to $Au_{0.79}Ag_{0.21}$ and thereby possesses higher antibacterial activity.

In vitro biofilm formation assay

The inhibition of biofilm formation by $Au_{0.91}Ag_{0.09}$, $Au_{0.79}Ag_{0.21}$, and AgNPs-PVP was studied with a static microtiter plate assay on *S. epidermidis,* Fig. 7 and Table S3. The samples $Au_{0.91}Ag_{0.09}$, $Au_{0.79}Ag_{0.21}$, and AgNPs-PVP were significantly able to hinder *S. epidermidis* biofilm formation. Notably, Au–Ag NPs and in particular $Au_{0.91}Ag_{0.09}$ NPs showed more inhibition when compared with the control. Therefore, these results point out that AgNPs demonstrate strong
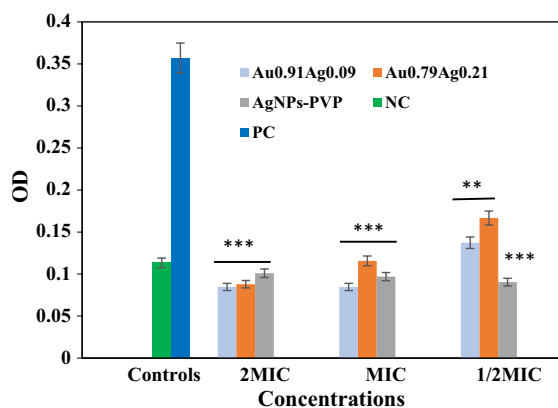

Fig. 7 a Histogram representing biofilm inhibition at OD 590 nm after treatment with $Au_{0.91}Ag_{0.09}$, $Au_{0.79}Ag_{0.21}$, and AgNPs-PVP for 48 h at 2 MIC, MIC, and ½ MIC compared with the positive and negative controls, which showed inhibition of *S. epidermidis* biofilm formation. Values are expressed mean ± SD (n = 3). Statistical analysis was performed using the paired Student t test. P values < 0.05 were considered significant. Double stars $0.001 < P < 0.01$ and triple stars $P < 0.001$

bactericidal activity as well as antibiofilm activity by low absorbance values (Murzyn et al. 2010).

In conclusion, the toxicity caused by metal NPs towards bacterial cells depends on their physical and chemical properties (Liu et al. 2014; Jena et al. 2020). Dong et al. reported different particle sizes and concentrations that can affect the bacterial cells and concluded that the smaller the size of AgNPs the higher their antibacterial activity (Dong et al. 2019). In another study by Ramasamy et al., it was shown that very small and spherical Au–Ag NPs infiltrated through the biofilms and repressed the entire bacterial populations even at low concentrations (Ramasamy et al. 2016). Recently, Liu et al. discoursed the release of Ag ions and their routes for antibacterial action (Xu et al. 2021). In our study, we can see the size dependence of the antibacterial effects. Both DLS and TEM sizes are smaller for $Au_{0.91}Ag_{0.09}$ than $Au_{0.79}Ag_{0.21}$. The smaller size alloy NPs presented higher antibacterial. In addition, less ratio of Ag is more potent antibacterial in solution. Taken together, the sizes of nanoparticles after dispersion in water are below the critical size of 100 nm. Table 2 presents the negative zeta potential of all samples. Sample $Au_{0.91}Ag_{0.09}$ of higher antibacterial effect has a lower Ag ratio, smaller size, and higher negative zeta potential than $Au_{0.79}Ag_{0.21}$.

Conclusions

Bimetallic $Au_{0.91}Ag_{0.09}$ and $Au_{0.79}Ag_{0.21}$ NPs were synthesized using the galvanic replacement method. The exchange is feasible given the facile reduction of aryldiazonium gold(III) salts at a potential comparable with the oxidation of AgNPs. The isolated Au–Ag NPs are highly stable in high NaCl concentration compared with pure AgNPs. Dissolution tests were monitored, and Ag showed low dissolution from the alloys. Hence, a size-dependent effect on the antimicrobial function was observed in this study. Smaller-size alloy NPs produce more Ag ions in water due to larger surface area and are more antibacterial. Our data suggest that the average size of Au–Ag NPs is a key factor in the determination of their antibacterial efficiency. Moreover, less Ag ratio presented higher potent antibacterial effects. Overall, oxidative leaching of Ag and hence their bioavailability in the media are indicators of the antibacterial effects.

Data availability The data used to support the findings of this study are included within the article.

Declarations

Competing interest The authors declare that they have no known competing financial interests or personal relationships that could have appeared to influence the work reported in this paper.

References

Ahmad AAL, Panicker S, Chehimi MM, Monge M, Lopez-De-Luzuriaga JM, Mohamed AA, Bruce AE, Bruce MRM (2019) Synthesis of water-soluble gold-aryl nanoparticles with distinct catalytic performance in the reduction of the environmental pollutant 4-nitrophenol. Catal Sci Technol 9:6059–6071. https://doi.org/10.1039/c9cy01402k

Al-Zubeidi A, Stein F, Flatebo C, Rehbock C, Hosseini Jebeli SA, Landes CF, Barcikowski S, Link S (2021) Single-particle hyperspectral imaging reveals kinetics of silver ion leaching from alloy nanoparticles. ACS Nano 15:8363–8375

Au L, Lu X, Xia Y (2008) A comparative study of galvanic replacement reactions involving Ag nanocubes and AuCl2− or AuCl4−. Adv Mater 20:2517–2522

Bai T, Tan Y, Zou J, Nie M, Guo Z, Lu X, Gu N (2015) AuBr 2−-engaged galvanic replacement for citrate-capped Au–Ag alloy nanostructures and their solution-based surface-enhanced raman scattering activity. J Phys Chem C 119:28597–28604

Berahim N, Basirun WJ, Leo BF, Johan MR (2018) Synthesis of bimetallic gold-silver (Au-Ag) nanoparticles for the catalytic reduction of 4-nitrophenol to 4-aminophenol. Catalysts 8:412

Bhattacharya C, Arora N, Jagirdar BR (2018) Digestive-ripening-facilitated nanoengineering of diverse bimetallic nanostructures. Langmuir 35:6493–6505

Bijalwan K, Kainthola A, Sharma H, Dwivedi C (2020) Catalytic reduction of 4-nitrophenol using gold-silver alloy nanoparticles coated on alkali activated sand. Mater Today Proc 28:1097–1100

Borah R, Verbruggen SW (2020) Silver-gold bimetallic alloy versus core-shell nanoparticles: implications for plasmonic enhancement and photothermal applications. J Phys Chem C 124:12081–12094

Botros NS (2015) Gold in Egypt: does the future get worse or better? Ore Geol Rev 67:189–207

Chen L, Deming CP, Peng Y, Hu P, Stofan J, Chen S (2016) Gold core@ silver semishell Janus nanoparticles prepared by interfacial etching. Nanoscale 8:14565–14572

Chernousova S, Epple M (2013) Silver as antibacterial agent: ion, nanoparticle, and metal. Angew Chemie Int Ed 52:1636–1653

Cunningham JC, Kogan MR, Tsai Y-J, Luo L, Richards I, Crooks RM (2016) based sensor for electrochemical detection of silver nanoparticle labels by galvanic exchange. ACS Sens 1:40–47

Das S, Debnath N, Mitra S, Datta A, Goswami A (2012) Comparative analysis of stability and toxicity profile of three differently capped gold nanoparticles for biomedical usage. Biometals 25:1009–1022

Dolinska J, Holdynski M, Ambroziak R, Modrzejewska-Sikorska A, Milczarek G, Pisarek M, Opallo M (2020) The medium effect on electrodissolution of adsorbed or suspended Ag nanoparticles. Electrochim Acta 350:136406

Dong Y, Zhu H, Shen Y, Zhang W, Zhang L (2019) Antibacterial activity of silver nanoparticles of different particle size against Vibrio Natriegens. PLoS ONE 14:e0222322

Ferrando R, Jellinek J, Johnston RL (2008) Nanoalloys: from theory to applications of alloy clusters and nanoparticles. Chem Rev 108:845–910

Gilroy KD, Hughes RA, Neretina S (2014) Kinetically controlled nucleation of silver on surfactant-free gold seeds. J Am Chem Soc 136:15337–15345

Gilroy KD, Ruditskiy A, Peng H-C, Qin D, Xia Y (2016) Bimetallic nanocrystals: syntheses, properties, and applications. Chem Rev 116:10414–10472

González E, Arbiol J, Puntes VF (2011) Carving at the nanoscale: sequential galvanic exchange and Kirkendall growth at room temperature. Science 334:1377–1380

Hahn A, Fuhlrott J, Loos A, Barcikowski S (2012) Cytotoxicity and ion release of alloy nanoparticles. J Nanoparticle Res 14:1–10

Han C, Likodimos V, Khan JA, Nadagouda MN, Andersen J, Falaras P, Rosales-Lombardi P, Dionysiou DD (2014) UV–visible light-activated Ag-decorated, monodisperse TiO$_2$ aggregates for treatment of the pharmaceutical oxytetracycline. Environ Sci Pollut Res 21:11781–11793

Han C, Nagendra V, Baig RB, Varma RS, Nadagouda MN (2015) Expeditious synthesis of noble metal nanoparticles using vitamin B12 under microwave irradiation. Appl Sci 5:415–426

Holt LR, Plowman BJ, Young NP, Tschulik K, Compton RG (2016) The electrochemical characterization of single core–shell nanoparticles. Angew Chem Int Ed 55:397–400

Ivask A, ElBadawy A, Kaweeteerawat C, Boren D, Fischer H, Ji Z, Chang CH, Liu R, Tolaymat T, Telesca D (2014) Toxicity mechanisms in *Escherichia coli* vary for silver nanoparticles and differ from ionic silver. ACS Nano 8:374–386

Jang H, Min D-H (2015) Spherically-clustered porous Au–Ag alloy nanoparticle prepared by partial inhibition of galvanic replacement and its application for efficient multimodal therapy. ACS Nano 9:2696–2703

Jena P, Bhattacharya M, Bhattacharjee G, Satpati B, Mukherjee P, Senapati D, Srinivasan R (2020) Bimetallic gold–silver nanoparticles mediate bacterial killing by disrupting the actin cytoskeleton MreB. Nanoscale 12:3731–3749

Kittler S, Greulich C, Diendorf J, Koller M, Epple M (2010) Toxicity of silver nanoparticles increases during storage because of slow dissolution under release of silver ions. Chem Mater 22:4548–4554

Kwon YJ, Son DH, Ahn SJ, Kim MS, Kim K (1994) Vibrational spectroscopic investigation of benzoic acid adsorbed on silver. J Phys Chem 98:8481–8487

Li X, Chen Q, McCue I, Snyder J, Crozier P, Erlebacher J, Sieradzki K (2014) Dealloying of noble-metal alloy nanoparticles. Nano Lett 14:2569–2577

Link S, Wang ZL, El-Sayed MA (1999) Alloy formation of gold−silver nanoparticles and the dependence of the plasmon absorption on their composition. J Phys Chem B 103:3529–3533

Liu J, Sonshine DA, Shervani S, Hurt RH (2010) Controlled release of biologically active silver from nanosilver surfaces. ACS Nano 4:6903–6913

Liu T, Song X, Guo Z, Dong Y, Guo N, Chang X (2014) Prolonged antibacterial effect of silver nanocomposites with different structures. Colloids Surf B 116:793–796

Liu R, Guo J, Ma G, Jiang P, Zhang D, Li D, Chen L, Guo Y, Ge G (2016) Alloyed crystalline Au–Ag hollow nanostructures with high chemical stability and catalytic performance. ACS Appl Mater Interfaces 8:16833–16844

Long Y-M, Hu L-G, Yan X-T, Zhao X-C, Zhou QF, Cai Y, Jiang GB (2017) Surface ligand controls silver ion release of nanosilver and its antibacterial activity against *Escherichia coli*. Int J Nanomed 12:3193

Loza K, Heggen M, Epple M (2020) Synthesis, structure, properties, and applications of bimetallic nanoparticles of noble metals. Adv Funct Mater 30:1909260

Ma R, Levard C, Marinakos SM, Cheng Y, Liu J, Michel FM, Brown GE Jr, Lowry GV (2012) Size-controlled dissolution of organic-coated silver nanoparticles. Environ Sci Technol 46:752–759

Mao H, Feng J, Ma X, Wu C, Zhao X (2012) One-dimensional silver nanowires synthesized by self-seeding polyol process. J Nanoparticle Res 14:1–15

Martínez LL, Segarra M, Fernandez M, Espiell F (1993) Kinetics of the dissolution of pure silver and silver-gold alloys in nitric acid solution. Metall Trans B 24:827–837

Mijnendonckx K, Leys N, Mahillon J, Silver S, Van Houdt R (2013) Antimicrobial silver: uses, toxicity and potential for resistance. Biometals 26:609–621

Mohamed AA, Bruce AE, Bruce MRM (1999) Cyclic voltammetry of Auranofin. Met-Based Drugs 6:233–238

Mohamed AA, Bauer JAK, Bruce AE, Bruce MRM (2003) [μ-o-Phenylenebis (diphenylphosphine)-κ2P: P′] bis [chlorogold (I)], dppbz (AuCl)$_2$. Acta Crystallogr C 59:m84–m86

Murzyn A, Krasowska A, Stefanowicz P, Dziadkowiec D, Łukaszewicz M (2010) Capric acid secreted by *S. boulardii* inhibits *C. albicans* filamentous growth, adhesion and biofilm formation. PLoS ONE 5(8):12050

Nishimura S, Dao ATN, Mott D, Ebitani K, Maenosono S (2012) X-ray absorption near-edge structure and X-ray photoelectron spectroscopy studies of interfacial charge transfer in gold–silver–gold double-shell nanoparticles. J Phys Chem C 116:4511–4516

Padmos JD, Langman M, MacDonald K, Comeau P, Yang Z, Filiaggi M, Zhang P (2015) Correlating the atomic structure of bimetallic silver–gold nanoparticles to their antibacterial and cytotoxic activities. J Phys Chem C 119:7472–7482

Pagannone M, Fornari B, Mattei G (1987) Molecular structure and orientation of chemisorbed aromatic carboxylic acids: surface enhanced Raman spectrum of benzoic acid adsorbed on silver sol. Spectrochim Acta Part A 43:621–625

Pallavicini P, Taglietti A, Dacarro G, Diaz-Fernandez YA, Galli M, Grisoli P, Patrini M, De Magistris GS, Zanoni R (2010) Self-assembled monolayers of silver nanoparticles firmly grafted on glass surfaces: Low Ag+ release for an efficient antibacterial activity. J Colloid Interface Sci 350:110–116

Panicker S, Ahmady IM, Han C, Chehimi M, Mohamed AA (2020) On demand release of ionic silver from gold-silver alloy nanoparticles: fundamental antibacterial mechanisms study. Mater Today Chem 16:100237. https://doi.org/10.1016/j.mtchem.2019.100237

Pattadar DK, Sharma JN, Mainali BP, Zamborini FP (2019) Impact of the assembly method on the surface area-to-volume ratio and electrochemical oxidation potential of metal nanospheres. J Phys Chem C 123:24304–24312

Peretyazhko TS, Zhang Q, Colvin VL (2014) Size-controlled dissolution of silver nanoparticles at neutral and acidic pH conditions: kinetics and size changes. Environ Sci Technol 48:11954–11961

Plowman BJ, Sidhureddy B, Sokolov SV, Young NP, Chen A, Compton RG (2016) Electrochemical behavior of gold–silver alloy nanoparticles. ChemElectroChem 3:1039–1043

Ramasamy M, Lee J-H, Lee J (2016) Potent antimicrobial and antibiofilm activities of bacteriogenically synthesized gold–silver nanoparticles against pathogenic bacteria and

their physiochemical characterizations. J Biomater Appl 31:366–378

Ray P, Clément M, Martini C, Abdellah I, Beaunier P, Rodriguez-Lopez JL, Huc V, Remita H, Lampre I (2018) Stabilisation of small mono-and bimetallic gold–silver nanoparticles using calix [8] arene derivatives. New J Chem 42:14128–14137

Rioux D, Meunier M (2015) Seeded growth synthesis of composition and size-controlled gold–silver alloy nanoparticles. J Phys Chem C 119:13160–13168

Russo L, Puntes V, Merkoçi A (2018) Tunable electrochemistry of gold-silver alloy nanoshells. Nano Res 11:6336–6345

Saw EN, Grasmik V, Rurainsky C, Epple M, Tschulik K (2016) Electrochemistry at single bimetallic nanoparticles–using nano impacts for sizing and compositional analysis of individual AgAu alloy nanoparticles. Faraday Discuss 193:327–338

Shibata T, Bunker BA, Zhang Z, Meisel D, Vardeman CF, Gezelter JD (2002) Size-dependent spontaneous alloying of Au− Ag nanoparticles. J Am Chem Soc 124:11989–11996

Shirman T, Lattimer J, Luneau M et al (2018) New architectures for designed catalysts: selective oxidation using agau nanoparticles on colloid-templated silica. Chem Eur J 24:1833–1837

Sun Y, Wang Y (2011) Monitoring of galvanic replacement reaction between silver nanowires and HAuCl4 by in situ transmission X-ray microscopy. Nano Lett 11:4386–4392

Sun Y, Xia Y (2004) Mechanistic study on the replacement reaction between silver nanostructures and chloroauric acid in aqueous medium. J Am Chem Soc 126:3892–3901

Sun Y, Mayers BT, Xia Y (2002) Template-engaged replacement reaction: a one-step approach to the large-scale synthesis of metal nanostructures with hollow interiors. Nano Lett 2:481–485

Tanner EEL, Sokolov SV, Young NP, Batchelor-McAule C, Compton RG (2017a) Fluorescence electrochemical microscopy: capping agent effects with ethidium bromide/DNA capped silver nanoparticles. Angew Chem 129:12925–12928

Tanner EEL, Sokolov SV, Young NP, Compton RG (2017b) DNA capping agent control of electron transfer from silver nanoparticles. Phys Chem Chem Phys 19:9733–9738

Toh HS, Jurkschat K, Compton RG (2015) The Influence of the capping agent on the oxidation of silver nanoparticles: nano-impacts versus stripping voltammetry. Chem Eur J 21:2998–3004

Wan D, Xia X, Wang Y, Xia Y (2013) Robust synthesis of gold cubic nanoframes through a combination of galvanic replacement, gold deposition, and silver dealloying. Small 9:3111–3117

Wang S, Li Q, Kang X, Zhu M (2018) Customizing the structure, composition, and properties of alloy nanoclusters by metal exchange. Acc Chem Res 51:2784–2792

Wikler MA (2006) Methods for dilution antimicrobial susceptibility tests for bacteria that grow aerobically: approved standard. CLSI 26:M7-A7

Wu T, Ma J, Wang X, Liu Y, Xu H, Gao J, Wang W, Liu Y, Yan J (2013) Graphene oxide supported Au–Ag alloy nanoparticles with different shapes and their high catalytic activities. Nanotechnology 24:125301

Xie R-C, Batchelor-McAuley C, Yang M, Compton RG (2021) Substrate mediated dissolution of redox active nanoparticles; electron transfer over long distances. Nano Res 1–9

Xie R-C, Batchelor-McAuley C, Yang M, Compton RG (2022) Substrate mediated dissolution of redox active nanoparticles; electron transfer over long distances. Nano Res 15:429–437

Xu Z, Zhang C, Wang X, Liu D (2021) Release strategies of silver ions from materials for bacterial killing. ACS Appl Bio Mater 4:3985–3999

Yang L, Yan W, Wang H, Zhuang H, Zhang J (2017) Shell thickness-dependent antibacterial activity and biocompatibility of gold@ silver core–shell nanoparticles. RSC Adv 7:11355–11361

Yu KH, Rhee JM, Lee Y, Lee K, Yu SC (2001) Surface-enhanced Raman scattering study of 4-biphenylcarboxylic acid. Langmuir 17:52–55

Zhang W, Yao Y, Sullivan N, Chen Y (2011) Modeling the primary size effects of citrate-coated silver nanoparticles on their ion release kinetics. Environ Sci Technol 45:4422–4428

Zheng K, Xie J (2020) Composition-dependent antimicrobial ability of full-spectrum Au x Ag25–x alloy nanoclusters. ACS Nano 14:11533–11541

Zhou M, Li C, Fang J (2020) Noble-metal based random alloy and intermetallic nanocrystals: syntheses and applications. Chem Rev

Zugic B, Wang L, Heine C, Zakharov DN, Lechner BAJ, Stach EA, Biener J, Salmeron M, Madix RJ, Friend CM (2017) Dynamic restructuring drives catalytic activity on nanoporous gold–silver alloy catalysts. Nat Mater 16:558–564